Design and Optimization of a Novel Bored Biplanar Permanent Magnet Assembly for Hybrid MRI Systems

Tony Tadic[1,2], B. Gino Fallone[1,2,3]

[1]Department of Physics, University of Alberta, Edmonton, Alberta T6G 1Z2, Canada
[2]Department of Medical Physics, Cross Cancer Institute, Edmonton, Alberta T6G 1Z2, Canada
[3]Department of Oncology, University of Alberta, Edmonton, Alberta T6G 1Z2, Canada

A novel design is presented for a biplanar permanent magnet assembly suitable for use in hybrid magnetic resonance imaging (MRI) systems. The key feature of the proposed design is a large cylindrical hole that is longitudinally bored through the entire magnet assembly. The presence of the bore permits the potential inclusion of additional peripheral devices within or near the magnet structure that may benefit from being placed along, or oriented parallel to, the main magnetic field. In particular, the magnet assembly is considered for use in an integrated system consisting of a 6 MV medical linear accelerator (linac) coupled to an MRI system for state of the art real-time image-guided adaptive radiotherapy. Magnetic field calculations based on the finite element method (FEM) are used to quantify the detrimental effects of the bore on the field homogeneity in the imaging volume for pole piece designs found commonly in industry. Shape optimization of the pole pieces is then demonstrated to yield novel pole designs that lead to suitable levels of field homogeneity. The resultant magnetic field within the bore is examined for the optimized design exhibiting maximum field homogeneity.

***Index Terms*— Geometrical parameterization, image-guided radiotherapy, magnetic field homogeneity, magnetic resonance imaging (MRI), non-axisymmetric, permanent magnet, shape optimization.**

I. Introduction

MAGNETIC RESONANCE imaging (MRI) is a powerful non-invasive biomedical technique capable of producing high quality images with exceptional soft-tissue contrast. Recent advancements in MRI technology coupled with the ability to perform functional and spectroscopic imaging have contributed to the rapidly growing popularity of this imaging modality.

MRI systems generally employ permanent, resistive, or superconducting magnets to produce a strong homogeneous static magnetic field B_0 that uniformly polarizes the nuclear magnetic spins of the subject examined. Superconducting magnets offer the greatest field strengths and highest image quality, thus optimizing the design of these systems has been of great interest [1]-[12]. Resistive magnets produce weaker field strengths than superconducting systems, but they are less expensive and exhibit smaller fringe fields. As a result, optimal design methods for compact resistive magnets have also been pursued [13]-[16]. Unfortunately, resistive and superconducting magnets require dedicated cooling and power systems, and are relatively expensive to build and operate. Consequently, permanent magnet systems are emerging as a viable alternative in low-field MRI applications, due to their relatively low weight, size, and cost. Resistive and superconducting magnet designs are typically based on cylindrical or split-coil windings, therefore these systems are restricted in terms of their possible geometrical configurations [17]. In comparison, a large variety of open and compact permanent magnet geometries can be found [18]-[26]. Advancements in permanent magnet design optimization [18], [27]-[37], and post-manufacturing passive shimming [38]-[41], have opened the door for magnet designers to pursue new and unique permanent magnet configurations tailored to specific applications.

FIG. 1 HERE

In this work, a design is proposed for a novel biplanar permanent magnet structure with a large cylindrical hole longitudinally bored through the entire assembly. The structure geometry is based on a four-column design as first presented in [27]. The existence of the bore permits the inclusion of additional therapeutic or diagnostic devices within or proximate to the magnet structure that might benefit from being directed along, or oriented parallel to, the main magnetic field of the MRI system. In particular, this magnet structure is considered a candidate for use in an integrated medical linear accelerator (linac) and MRI system capable of performing real-time image-guided adaptive radiotherapy.

The use of a biplanar permanent magnet in the design of an integrated linac-MRI system was first proposed by our group in [42], [43]. In the initial design of this system, a 6 MV linac was coupled to the open end of a 0.2 T permanent magnet assembly such that the linac and x-ray beam were oriented perpendicular to the main magnetic field. It was later reported that this transverse arrangement of the x-ray beam with respect to the main magnetic field leads to the production of unfavourable hot and cold spots at tissue-air interfaces in the resultant treatment plans at high field strengths [44]. Recently, an alternative arrangement was proposed by our group in which the linac and x-ray beam were oriented parallel to the main magnetic field [45]. It has been shown that this parallel arrangement is advantageous in that it leads to a reduction of the aforementioned hot and cold spots observed with the transverse arrangement [45], [46]. A schematic diagram illustrating both arrangements is shown in Fig 1.

In order for a biplanar permanent magnet system to permit a parallel arrangement, a large hole needs to be vacated from the magnet assembly in order to provide an unobstructed beam path for the linac. It is expected that the presence of such a

hole would affect the characteristics of the magnetic field in the imaging volume and thus impact the quality of images produced by this system. Consequently, an investigation into the viability of a bored biplanar permanent magnet for MRI is necessary so that the desired parallel arrangement can be pursued. Furthermore, the proper functioning of a linac device may be affected by the presence of external magnetic fields through interactions with the accelerating electrons in the waveguide interior. Detailed characterization of the magnetic field produced by the magnet system at potential linac locations is required so that a complete simulation of the electron dynamics in the waveguide can be performed.

In this paper, the finite element method (FEM) is employed to quantify the effects of the large bore on the magnetic field homogeneity in the imaging volume. It is verified that flat or single-ring annular shimmed (SRAS) pole pieces, as found commonly in industry, are inadequate in yielding suitable levels of field homogeneity for medical imaging [27], [30], [32], [35]. Accordingly, the optimization scheme previously presented in [37] is adapted to yield a novel optimized double-ring annular shimmed (DRAS) pole piece, as well as optimized axisymmetric and non-axisymmetric grid parameterized (AGP and NAGP) pole pieces. The method employed is similar in philosophy to the target-field approach presented in [47] for the design of circular biplanar gradient and shim coils, which relies on analytical field expressions valid in the absence of magnetic materials. In addition, the axisymmetric designs obtained are similar to the strictly axisymmetric solutions presented in [27], [35] for permanent magnet assemblies without a large bore.

Magnetic field inhomogeneities corresponding to the various pole piece designs are compared and the necessity of the optimized DRAS, AGP, and NAGP designs is demonstrated. The transverse and longitudinal magnetic fields produced by the magnet assembly with the NAGP optimized design are then examined within and proximate the large bore, providing insight towards the necessary details required in designing an integrated linac-MRI system with a parallel arrangement.

FIG. 2 HERE

II. Finite Element Method Problem Formulation

The magnetic field calculations required in this work are performed with the 3-D FEM software package COMSOL MULTIPHYSICS (version 3.4, Comsol AB, Stockholm, Sweden). Details of the FEM analysis have been provided in [37] and are reproduced here. The FEM problem formulation begins with Maxwell's equations in a current free region:

$$\nabla \times \boldsymbol{H} = 0 \tag{1-a}$$

$$\nabla \cdot \boldsymbol{B} = 0 \tag{1-b}$$

where $\boldsymbol{H}$ is the magnetic field vector and $\boldsymbol{B}$ is the magnetic flux density. Due to the absence of currents, $\boldsymbol{H}$ can be expressed in terms of the gradient of a scalar potential V_m:

$$\boldsymbol{H} = -\nabla V_m . \tag{2}$$

In a region with magnetic permeability μ and magnetization $\boldsymbol{M}$, the fields $\boldsymbol{H}$ and $\boldsymbol{B}$ are related by:

$$\boldsymbol{B} = \mu(\boldsymbol{H} + \boldsymbol{M}) . \tag{3}$$

Combining (1-a), (1-b), (2), and (3) yields:

$$\nabla \cdot (\mu \nabla V_m - \mu \boldsymbol{M}) = 0 . \tag{4}$$

The magnetostatics application mode in the AC/DC module of COMSOL MULTIPHYSICS is employed to numerically solve (4) for V_m at discrete points within the model geometry, subject to appropriate boundary conditions. The fields $\boldsymbol{H}$ and $\boldsymbol{B}$ can then be calculated directly by (2) and (3), respectively.

Convergence is achieved in solving the nonlinear problem (4) when the specified relative tolerance of 10^{-6} exceeds the relative error estimate, which is computed as a weighted Euclidean norm of the estimated nodal error values in V_m [48]. Tetrahedral quadratic Lagrange elements are used to partition the model geometry in order to obtain an accurate piecewise linear solution for $\boldsymbol{H}$ and $\boldsymbol{B}$ without excessive computational burden.

III. A Novel Bored Permanent Magnet Assembly

The bored four-column biplanar permanent magnet assembly considered in this work is shown in Fig. 2. This magnet assembly is identical to the reduced magnet structure analyzed in [37] with the exception of a large 20 cm diameter longitudinal hole bored through the center of the entire magnet assembly. Table I provides values for the dimensions labeled in Fig. 2(b), where the minimum pole separation g is chosen as 70 cm to allow for rotation around a typical human patient.

The FEM calculations take into account the nonlinearity of the AISI 1020 plain carbon steel yoke and column structures, and the Armco magnetic steel pole pieces, through the relative permeability functions shown in Fig. 3 [37], [49], [50]. Additionally, the residual flux density of the Nd-Fe-B permanent magnet poles is chosen as 1.005 T.

TABLE 1 HERE

FIG. 3 HERE

In order to compare various magnet assembly designs, the inhomogeneity PPM_V of the magnetic field measured over the volume of interest V is introduced as a value of merit:

$$PPM_V = \frac{B_{\max} - B_{\min}}{B_0} \times 10^6 \tag{5}$$

where $B_{\max}$ and $B_{\min}$ are the maximum and minimum values for the magnetic flux density magnitude within V, respectively, and B_0 is the magnetic flux density magnitude at isocenter.

Table II compares the magnetic field properties for the magnet assemblies with and without the 20 cm bore. B_0 and PPM_V values are presented for each system for both flat and SRAS pole pieces. The definition of the objective function Ψ appearing in Table II is provided later in Section V. The width and depth of the peripheral ring of the SRAS pole pieces have been optimized to achieve maximum field homogeneity within a 40 cm diameter spherical volume (DSV) at isocenter for both cases. Details of this optimization procedure are provided in Sections IV and V.

The effect of the large bore is to reduce the field at isocenter B_0 as the amount of magnetic material in the assembly that contributes to the net magnetic field at this point is reduced. This reduction is especially significant for the design with the SRAS pole piece; the optimized peripheral ring has greater depth in the bored system, resulting in a further reduction of magnetic material as compared to the standard system without the bore.

The presence of the bore also leads to a dramatic increase in the PPM_V inhomogeneity for both flat and SRAS pole piece designs. Based on the assumption that successful post-manufacturing shimming of a magnet assembly requires an inhomogeneity value of less than 300 ppm in the imaging volume of interest, the bored magnet systems examined here are considered unsuitable for medical imaging over both 30 and 40 cm DSVs.

TABLE 2 HERE

IV. Geometric Parameterization of the Design Surface

A. Annular Shimmed Parameterization

The open face of the magnetic pole piece of the bored magnet assembly is taken as the design surface. The design variables are selected as the dimensions of the pole piece cross section, as shown for the upper pole piece in Fig. 4. This results in 5 unique design variables for the DRAS design, and 3 unique design variables for the SRAS design with the constraint $z_4 = z_5 = 0$.

B. Grid Parameterization

For the grid-based designs, the open face of the magnetic pole piece is parameterized with 112 control points distributed on the polar grid shown in Fig. 5. This parameterization is similar to that used in [37], with the appropriate adjustments in order to account for the presence of the bore. The z coordinates of the control points are taken as the design variables so that the thickness of the pole piece at each of these locations is varied during optimization. The complete pole piece surface is then generated based on a linear spline interpolation between the control points, similar to the Bezier spline approach in [35].

Particular symmetry in the pole piece surface allows for constraints to be imposed on the control points in order to reduce the number of design variables [37]. When seeking AGP pole piece designs, only those control points on the line ($\theta = 0$) are considered unique, resulting in a total of 7 unique design variables during optimization. When permitting NAGP designs, only those control points on the lines ($\theta = 0$, $\pi/8$, $\pi/4$) are considered unique, resulting in a total of 21 unique design variables.

FIG. 4 HERE

FIG. 5 HERE

V. Nonlinear Optimization Algorithm

Details of the iterative optimization process have been presented in [37] and are reproduced here. The major steps of the iterative scheme are summarized in the flow diagram of Fig. 6. The algorithm is scripted in MATLAB (version 7.5, The MathWorks Inc., Natick, MA) and utilizes macros from the COMSOL MULTIPHYSICS scripting language. The optimization can be expressed as:

$$\text{Minimize } \Psi = f(\boldsymbol{p}) \tag{6-a}$$

$$\text{Subject to } p_{min} \le p_i \le p_{max}, \quad \text{for } i = 1, \ldots, N \tag{6-b}$$

where Ψ is the objective function and $\boldsymbol{p}$ is the design vector. For N unique design variables, the elements of $\boldsymbol{p}$ are denoted p_i (for i = 1, …, N) and are subject to the lower and upper constraints p_{min} and p_{max}, respectively.

The objective function minimized during optimization is defined as:

$$\Psi = \int_{\Omega} \left(B(\boldsymbol{r}; \boldsymbol{p}) - B_0 \right)^2 \mathrm{d}\Omega' \tag{7}$$

where $B(\boldsymbol{r}; \boldsymbol{p})$ is the magnitude of the magnetic flux density at the point $\boldsymbol{r}$, implicitly due to the magnet design defined by $\boldsymbol{p}$. Therefore, Ψ is a cumulative measure of the magnetic field inhomogeneity in the volume Ω, which is chosen as a 40 cm DSV at isocenter. The gradient of the objective function $\nabla\Psi$ with respect to the design variables is defined as:

$$\nabla\Psi = \left[\frac{\partial \Psi}{\partial p_1} \quad \cdots \quad \frac{\partial \Psi}{\partial p_N} \right] \tag{8}$$

for which each of the partial derivatives is approximated using a forward finite difference approximation:

$$\frac{\partial \Psi}{\partial p_i} \cong \frac{\Psi(p_i + \delta p) - \Psi(p_i)}{\delta p} \tag{9}$$

with a perturbation size δp of 0.1 mm. In order to minimize (7), the design vector is updated at the kth iteration according to the well known steepest descent optimization method [51]:

$$\boldsymbol{p}^{k+1} = \boldsymbol{p}^k - \boldsymbol{\alpha}^k \nabla\Psi^k \tag{10}$$

where α is the step size determined by a simple bisection line search algorithm [52].

The iterative optimization process is repeated until convergence in the objective function is achieved.

FIG. 6 HERE

VI. Numerical Optimization Results

An optimized DRAS pole piece design was obtained after 186 iterations, while optimized AGP and NAGP designs were obtained after 672 and 1022 iterations, respectively. The resulting designs are visually compared in Fig. 7 alongside the flat and SRAS designs. Magnetic field properties for the various designs are tabulated and compared in Table II.

The greatest field uniformity is obtained with the NAGP design, which results in the lowest values for the objective function and inhomogeneity over both 30 and 40 cm DSVs. The performance and geometry of the AGP design is very similar to the NAGP design, with both designs now permitting post-manufacturing shimming and medical imaging over a 30 cm DSV. Evidently, the NAGP design does not provide a significant advantage over the AGP design, as the largest inhomogeneities present are those due to the bore and not the non-axisymmetric configuration of the yoke structure and columns.

The simple and effective DRAS design achieves significantly improved field inhomogeneity values compared to the flat and SRAS designs. Notably, it yields a 30cm DSV that is suitable for post-manufacturing shimming and medical imaging. Although the inhomogeneity values for this design are 2-3 times greater than the AGP and NAGP designs, the optimization requires significantly less computation time and the resulting design would be simpler to construct.

FIG. 7 HERE

VII. Magnetic Field Analysis

The magnetic field produced by the bored magnet assembly with the NAGP optimized pole piece design is analyzed in terms of its longitudinal B_z and transverse $B_\perp$ components within and proximate to the large bore. Longitudinal profiles passing through the bore are shown in Fig. 8 for a selection of positions along the x axis.

The various B_z profiles obtained are relatively similar in their shape and magnitude. A common trait of these profiles is a drop from the value near isocenter to a large negative value within the bore, followed by an increase to a small positive value that asymptotically approaches zero. The region of negative B_z within the bore corresponds to where the magnetic field reverses direction, as can be seen in the magnetic field line plot of Fig. 9.

In contrast, although the $B_\perp$ profiles retain a similar shape at various positions, the peak magnitude of this component changes dramatically. $B_\perp$ is zero on the z axis due to symmetry about the center of the bore, and increases in magnitude with increasing position along the x axis, as the bore edges are approached. This effect is illustrated in Fig. 8(c), which shows the peak magnitude of the transverse component within the bore volume as a function of distance s from the z axis. This field behaviour and the shape of the profiles are congruent with Fig 9, as the magnetic field reversal within the bore necessitates a change in the polarity of the transverse component as well.

FIG. 8 HERE

As the profiles indicate, the magnetic field within the bore is complex and highly inhomogeneous. In particular, both the longitudinal and transverse components reverse direction in this region, with the total field magnitude peaking at nearly 0.3 T. In comparison, the region exterior to the bore exhibits a weaker field with less variation and therefore may lend itself as a better candidate for the location of a magnetically sensitive device such as a linac. Although increasing the distance between the linac and isocenter would result in a reduction of the maximum achievable dose rate, this region is less confined and would better accommodate the necessary additional equipment and shielding required for actual linac operation. In any case, the complete three dimensional vector description of the magnetic field produced by the magnet assembly has been obtained and can now be used to simulate the electron dynamics of the linac waveguide in order to precisely evaluate its performance.

FIG. 9 HERE

VIII. Conclusion

The design and optimization of a novel bored biplanar permanent magnet assembly for MRI has been presented. A unique feature of this system is a large longitudinal hole that has been vacated from the magnet assembly to permit the inclusion of additional devices within or near the magnet structure that may be oriented along the direction of the main magnetic field. It has been demonstrated that the presence of the large bore degrades the magnetic field homogeneity in the imaging volume and therefore optimized pole piece designs are required. A complete description of the magnetic field produced by the magnet assembly has been obtained and will contribute to the further development of an integrated linac-MRI device with a parallel arrangement.

Acknowledgment

This work was supported in part by the Alberta Heritage Foundation for Medical Research and the Natural Sciences and Engineering Research Council of Canada.

References

[1] A. K. Kalafala, “A design approach for actively shielded magnetic resonance imaging magnets,” *IEEE Trans. Magn.*, vol. 26, no. 3, pp. 1181-1188, May 1990.

[2] S. Pissanetzky, “Structured coils for NMR applications,” *IEEE Trans. Magn.*, vol. 28, no. 4, pp. 1961-1968, July 1992.

[3] V. Cavaliere, A. Formisano, R. Martone, M. Primizia, "A genetic algorithm approach to the design of split coil magnets for MRI," *IEEE Trans. Appl. Supercond.*, vol. 10, no. 1, pp. 1376-1379, Mar. 2000.

[4] V. Cavaliere, A. Formisano, R. Martone, G. Masullo, A. Matrone, M. Primizia, "Design of split coil magnets for magnetic resonance imaging," *IEEE Trans. Appl. Supercond.*, vol. 10, no. 1, pp. 759-762, Mar. 2000.

[5] S. Besio, S. Pittaluga, V. Punzo, A. Trequattrini, "Elliptical coils for dedicated MRI magnets," *IEEE Trans. Appl. Supercond.*, vol. 18, no. 2, pp. 908-911, June 2008.

[6] G. Sinha, R. Sundararaman, G. Singh, "Design concepts of optimized MRI magnet," *IEEE Trans. Magn.*, vol. 44, no. 10, pp. 2351-2360, Oct. 2008.

[7] Q. M. Tieng, V. Vegh, I. M. Brereton, "Globally optimal superconducting magnets part I: minimum stored energy (MSE) current density map," *J. Magn. Reson.*, vol. 196, no. 1, pp. 1-6, Jan. 2009.

[8] Q. M. Tieng, V. Vegh, I. M. Brereton, "Globally optimal superconducting magnets part II: symmetric MSE coil arrangement," *J. Magn. Reson.*, vol. 196, no. 1, pp. 7-11, Jan. 2009.

[9] Q. Wang, G. Xu, Y. Dai, B. Zhao, L. Yan, K. Kim, "Design of open high magnetic field MRI superconducting magnet with continuous current and genetic algorithm method," *IEEE Trans. Appl. Supercond.*, vol. 19, no. 3, pp. 2289-2292, June 2009.

[10] Q. M. Tieng, V. Vegh, I. M. Brereton, "Minimum stored energy high-field MRI superconducting magnets," *IEEE Trans. Appl. Supercond.*, vol. 19, no. 4, pp. 3645-3652, Aug. 2009.

[11] M. Sekino, H. Ohsaki, H. Wada, T. Hisatsune, O. Ozaki, T. Kiyoshi, "Fabrication of an MRI model magnet with an off-centered distribution of homogeneous magnetic field zone," *IEEE Trans. Appl. Supercond.*, to be published.

[12] C. Wu, J. Guo, C. Chen, G. Yan, C. Li, "Optimal design and test of main magnet in superconducting MRI," *IEEE Trans. Appl. Supercond.*, to be published.

[13] A. Momy, J. Taquin, "Low-leakage wide-access magnet for MRI," *IEEE Trans. Magn.*, vol. 33, no. 6, pp. 4572-4574, Nov. 1997.

[14] P. N. Morgan, S. M. Conolly, A. Macovski, "Resistive homogeneous MRI magnet design by matrix subset selection," *Magn. Reson. Med.*, vol. 41, no. 6, pp. 1221-1229, June 1999.

[15] M. Sciandrone, G. Placidi, L. Testa, A. Sotgiu, "Compact low field magnetic resonance imaging magnet: design and optimization," *Rev. Sci. Instrum.*, vol. 71, no. 3, pp. 1534-1538, Mar. 2000.

[16] H. Xu, S. M. Conolly, G. C. Scott, A. Macovski, "Homogeneous magnet design using linear programming," *IEEE Trans. Magn.*, vol. 36, no. 2, pp. 476-483, Mar. 2000.

[17] Y. Lvovsky, P. Jarvis, "Superconducting systems for MRI- present solutions and new trends," *IEEE Trans. Appl. Supercond.*, vol. 15, no. 2, pp. 1317-1325, June 2005.

[18] A. Podol'skii, "Development of permanent magnet assembly for MRI devices," *IEEE Trans. Magn.*, vol. 34, no. 1, pp. 248-252, Jan. 1998.

[19] J. H. Jensen, M. G. Abele, "Generation of highly uniform magnetic fields with magnetized wedges," *IEEE Trans. Magn.*, vol. 34, no. 4, pp. 2316-2323, July 1998.

[20] J. H. Jensen, M. G. Abele, "Closed wedge magnets," *IEEE Trans. Magn.*, vol. 35, no. 5, pp. 4192-4199, Sept. 1999.

[21] A. Trequattrini, G. Coscia, S. Pittaluga, "Double-cavity open permanent magnet for dedicated MRI," *IEEE Trans. Appl. Supercond.*, vol. 10, no. 1, pp. 756-758, Mar. 2000.

[22] A. Podol'skii, "Permanent-magnet assemblies for magnetic resonance imaging devices for various purposes," *IEEE Trans. Magn.*, vol. 38, no. 3, pp. 1549-1552, May 2002.

[23] M. G. Abele, H. Rusinek, "Permanent conical magnet for interventional magnetic resonance imaging," *IEEE Trans. Magn.*, vol. 40, no. 5, pp. 3382-3386, Sept. 2004.

[24] Y. Yao, Y. Fang, C. S. Koh, G. Ni, "A new design method for completely open architecture permanent magnet for MRI," *IEEE Trans. Magn.*, vol. 41, no. 5, pp. 1504-1507, May 2005.

[25] A. Trequattrini, S. Besio, S. Pittaluga, V. Punzo, L. Satragno, "A novel 0.25 T dedicated MRI apparatus," *IEEE Trans. Appl. Supercond.*, vol. 16, no. 2, pp. 1505-1508, June 2006.

[26] Y. Zhang, D. Xie, B. Bai, H. S. Yoon, C. S. Koh, "New development of monohedral magnet for MRI using the combination of genetic algorithm and FEM-NESM," *IEEE Trans. Appl. Supercond.*, vol. 44, no. 6, pp. 1266-1269, June 2008.

[27] T. Miyamoto, H. Sakurai, H. Takabayashi, M. Aoki, "A development of a permanent magnet assembly for MRI devices using Nd-Fe-B material," *IEEE Trans. Magn.*, vol. 25, no. 5, pp. 3907-3909, Sept. 1989.

[28] M. G. Abele, J. H. Jensen, "Hybrid pole pieces for permanent magnets," *J. Appl. Phys.*, vol. 79, no. 8, pp. 5199-5201, Apr. 1996.

[29] J. H. Jensen, "Optimization method for permanent-magnet structures," *IEEE Trans. Magn.*, vol. 35, no. 6, pp. 4465-4472, Nov. 1999.

[30] A. Podol'skii, "Design procedure for permanent magnet assemblies with uniform magnetic fields for MRI devices," *IEEE Trans. Magn.*, vol. 36, no. 2, pp. 484-490, Mar. 2000.

[31] X. Jiang, G. Shen, Y. Lai, J.Tian, "Development of an open 0.3 T NdFeB MRI magnet," *IEEE Trans. Appl. Supercond.*, vol. 14, no. 2, pp. 1621-1623, June 2004.

[32] D.-H. Kim, B.-S. Kim, J.-H. Lee, W.-S. Nah, I.-H. Park, "3-D optimal shape design of ferromagnetic pole in MRI magnet of open permanent-magnet type," *IEEE Trans. Appl. Supercond.*, vol. 12, no. 1, pp. 1467-1470, Mar. 2002.

[33] Y. Yao, C. S. Koh, D. Xie, "Three-dimensional optimal shape design of magnetic pole in permanent magnet assembly for MRI taking account of eddy currents due to gradient coil field," *IEEE Trans. Magn.*, vol. 40, no. 2, pp. 1164-1167, Mar. 2004.

[34] D.-H. Kim, J. K. Sykulski, D. A. Lowther, "A novel scheme for material updating in source distribution optimization of magnetic devices using sensitivity analysis," *IEEE Trans. Magn.*, vol. 41, no. 5, pp. 1752-1755, May 2005.

[35] J. S. Ryu, Y. Yao, C. S. Koh, "3-D optimal shape design of pole piece in permanent magnet MRI using parameterized nonlinear design sensitivity analysis," *IEEE Trans. Magn.*, vol. 42, no. 4, pp. 1351-1354, Apr. 2006.

[36] M. G. Abele, W. Tsui, H. Rusinek, "Methodology of pole piece design in permanent magnets," *J. Appl. Phys.*, vol. 99, no. 8, Apr. 2006.

[37] T. Tadic, B. G. Fallone, "Three-dimensional non-axisymmetric pole piece shape optimization for biplanar permanent magnet MRI systems," submitted for publication.

[38] R. Vadovic, "Magnetic field correction using magnetized shims," *IEEE Trans. Magn.*, vol. 25, no. 4, pp. 3133-3139, July 1989.

[39] J. H. Battocletti, H. A. Kamal, T. J. Myers, T. A. Knox, "Systematic passive shimming of a permanent magnet for P-31 NMR spectroscopy of bone mineral," *IEEE Trans. Magn.*, vol. 29, no. 3, pp. 2139-2151, July 1993.

[40] H. S. Lopez, F. Liu, E. Weber, S. Crozier, "Passive shim design and a shimming approach for biplanar permanent magnetic resonance imaging magnets," *IEEE Trans. Magn.*, vol. 44, no. 3, pp. 394-402, Mar. 2008.

[41] Y. Zhang, D. Xie, B. Bai, H. S. Yoon, C. S. Koh, "A novel optimal design method of passive shimming for permanent MRI magnet," *IEEE Trans. Magn.*, vol. 44, no. 6, pp. 1058-1061, June 2008.

[42] B. G. Fallone, M. Carlone, B. Murray, S. Rathee, T. Stanescu, S. Steciw, *et al.*, "Development of a linac-MRI system for real-time ART," *Med. Phys.*, vol. 34, no. 6, pp. 2547-2547, June 2007.

[43] B. G. Fallone, B. Murray, S. Rathee, T. Stanescu, S. Steciw, S. Vidakovic, "First MR images obtained during megavoltage photon irradiation from a prototype integrated linac-MR system," *Med. Phys.*, vol. 36, no. 6, pp. 2084-2088, Apr. 2009.

[44] C. Kirkby, T. Stanescu, S. Rathee, M. Carlone, B. Murray, B. G. Fallone, "Patient dosimetry for hybrid MRI-radiotherapy systems," *Med. Phys.*, vol. 35, no. 3, pp. 1019-1027, Mar. 2008.

[45] B. G. Fallone, "Real-time MR-guided radiotherapy: integration of a low-field MR system," *Med. Phys.*, vol. 36, no. 6, pp. 2774-2775, June 2009.

[46] C. Kirkby, B. Murray, S. Rathee, B. G. Fallone, "Patient dosimetry in a linac-MR radiotherapy unit with a longitudinal magnetic field," *Med. Phys.*, to be published.

[47] L. K. Forbes, M. A. Brideson, S. Crozier, "A target-field method to design circular biplanar coils for asymmetric shim and gradient fields," *IEEE Trans. Magn.*, vol. 41, no. 6, pp. 2134-2144, June 2005.

[48] *Comsol Multiphysics Reference Guide,* ver. 3.4, Comsol AB, Stockholm, Sweden, 2007, pp. 501-502.

[49] N. B. S. Gloria, M. C. L. Areiza, I. V. J. Miranda, J. M. A. Rebello, "Development of a magnetic sensor for detection and sizing of internal pipeline corrosion defects," *NDT&E Int.*, vol. 42, no. 8, pp. 669-677, Dec. 2009.

[50] D. M. Kohler, "Production and properties of grain-oriented commercially pure iron," *J. Appl. Phys.*, vol. 38, no. 3, pp. 1176-1178, Mar. 1967.

[51] E. K. P. Chong, S. H. Zak, "Gradient methods," in *An Introduction to Optimization*, 3rd ed. New York: John Wiley & Sons, 2008, ch. 8, sec. 2, pp. 127-135.

[52] C. A. Floudas, P. M. Pardalos, “Bisection global optimization methods,” in *Encyclopedia of Optimization*, vol. 1, 1st ed. Dordrecht, Netherlands: Kluwer, 2001, pp. 186 – 189.

Tony Tadic was born in Edmonton, Alberta, Canada in 1984. He was awarded a Bachelor’s of Science degree in engineering physics from the University of Alberta in Edmonton, Alberta, Canada in 2006. He is currently pursuing a Doctor of Philosophy degree in medical physics at the University of Alberta and Cross Cancer Institute in Edmonton, Alberta, Canada.

He is currently a member of the Linac-MR research group at the Cross Cancer Institute, where efforts are being made to develop the world’s first hybrid integrated medical linear accelerator and magnetic resonance imager.

He is currently a student member of the American Association of Physicists in Medicine and the Canadian Organization of Medical Physicists.

TABLE I
BORED PERMANENT MAGNET ASSEMBLY DIMENSIONS

Quantity	Length (mm)
h	2066
g	700
w	1578
l	2600
d	1398
r	100

TABLE II
COMPARISON OF MAGNETIC FIELD PROPERTIES

Quantity	Standard Magnet Assembly		Bored Magnet Assembly				
	Flat Pole Piece	SRAS Pole Piece	Flat Pole Piece	SRAS Pole Piece	DRAS Pole Piece	Axisymmetric Optimized Pole Piece	Non-Axisymmetric Optimized Pole Piece
Iterations	-	11	-	75	186	672	1022
B_0 (T)	0.202	0.179	0.197	0.157	0.171	0.179	0.177
Ψ (10^{-11} T^2·m^3)	1440	1.895	647.1	19.51	1.685	0.719	0.353
$PPM_{30\text{cm DSV}}$	8734	321	7130	1355	279	180	77
$PPM_{40\text{cm DSV}}$	15232	1030	24978	4474	2116	1127	921

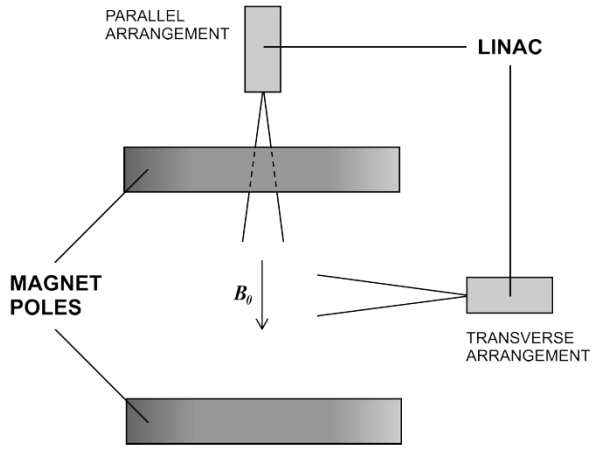

Fig. 1. Transverse and parallel arrangements for an integrated linac and biplanar magnet assembly.

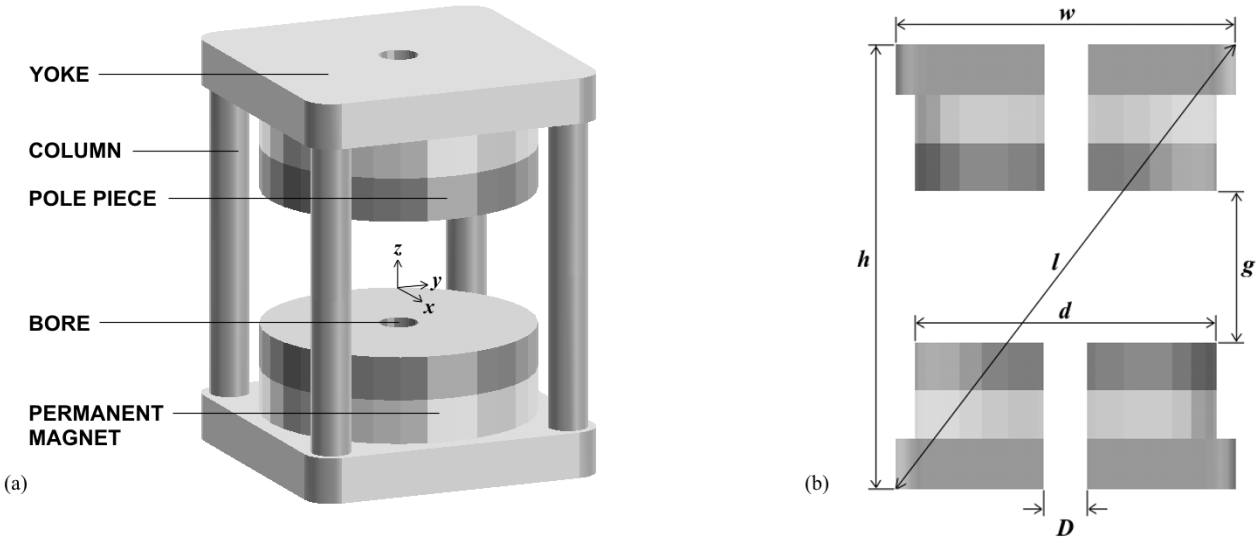

Fig. 2. (a) 3-D schematic of the novel bored biplanar permanent magnet assembly with coordinate axes and (b) a cross-sectional view with dimension labels.

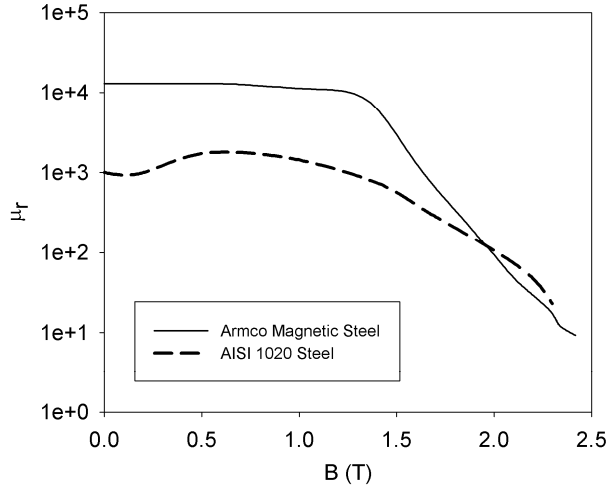

Fig. 3. Relative permeability functions for Armco magnetic steel and AISI 1020 plain carbon steel.

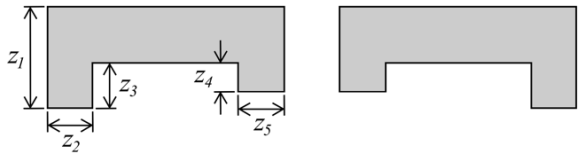

Fig. 4. Design parameterization for optimization of the SRAS and DRAS pole piece designs. Only the upper pole piece is illustrated.

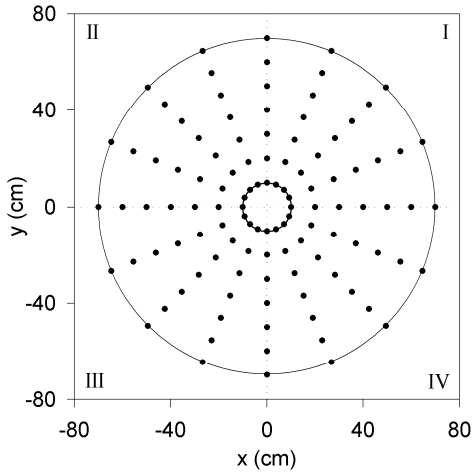

Fig. 5. Control point distribution for the AGP and NAGP pole piece designs, plotted in cartesian coordinates.

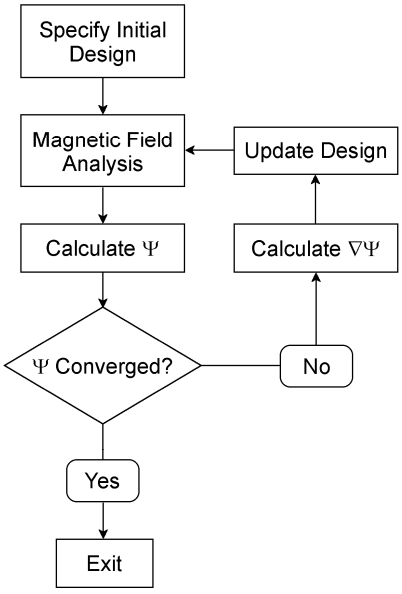

Fig. 6. Iterative optimization process flow diagram.

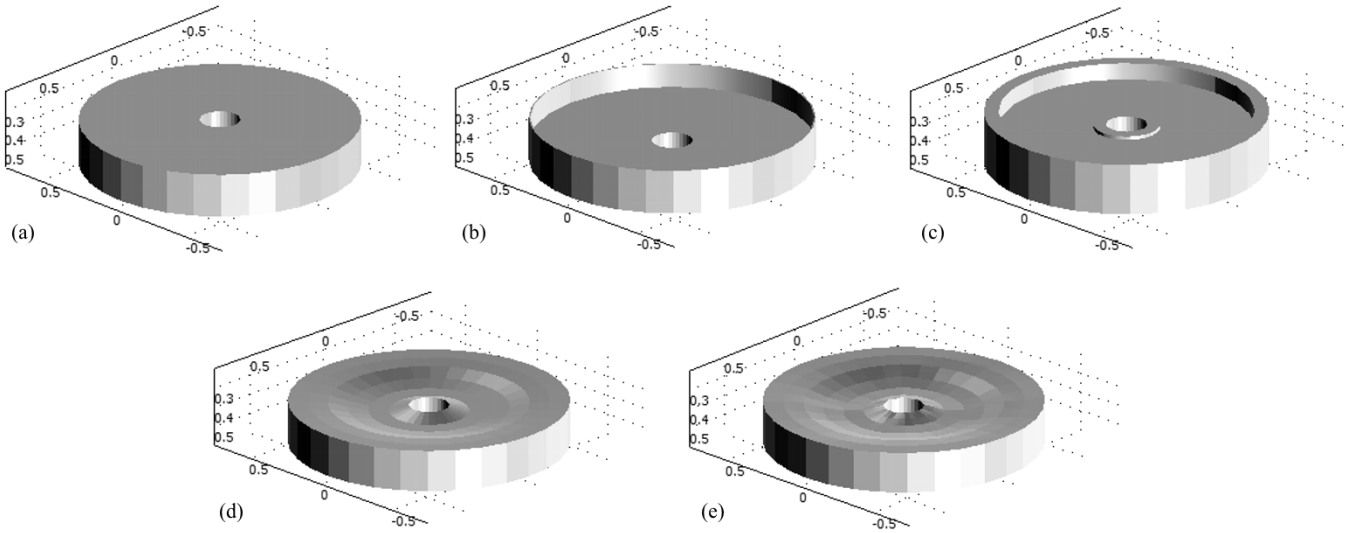

Fig. 7. 3-D visualizations of the (a) flat, (b) SRAS, (c) DRAS, (d) AGP, and (e) NAGP optimized pole pieces. Axis dimensions are displayed in meters.

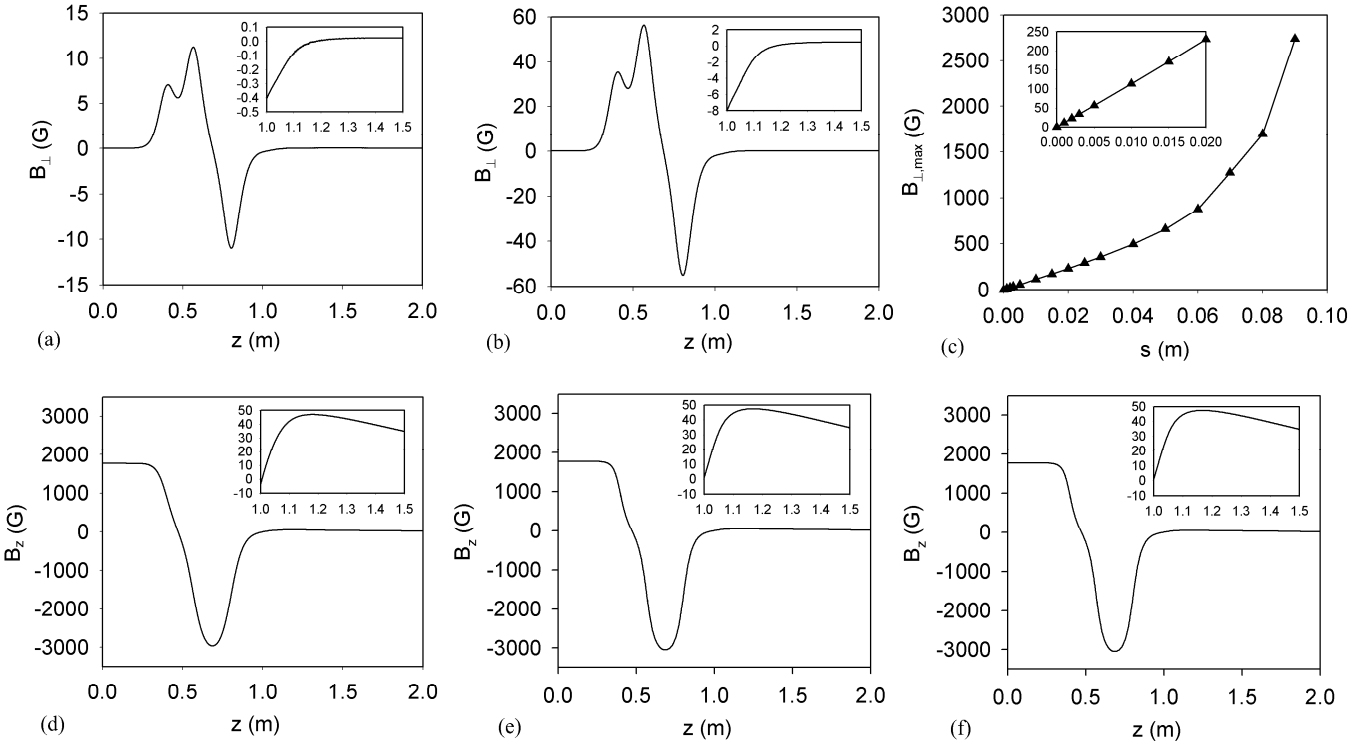

Fig. 8. $B_\perp$ profiles from the xz plane, taken at (a) x = 1 and (b) 5 mm. (c) The peak magnitude of $B_\perp$ within the bore volume, as a function of distance s from the z axis. B_z profiles from the xz plane, taken at (d) x = 0, (e) 5, and (f) 50 mm. Note that the bore volume extends from z = 0.35 to 1.033 m.

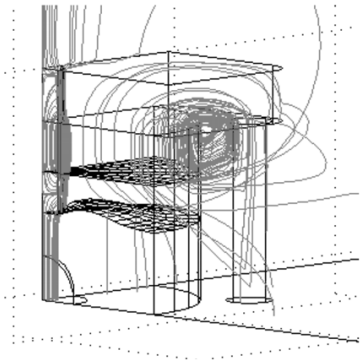

Fig. 9. Section of a 3-D magnetic field line plot illustrating the field reversal within the bore of the magnet assembly with the NAGP optimized pole piece.